ChemPhysChem

Research Article
doi.org/10.1002/cphc.202401050

Chemistry Europe
European Chemical Societies Publishing

www.chemphyschem.org

Identification of Adsorption Sites for CO_2 in a Series of Rare-Earth and Zr-Based Metal-Organic Frameworks

Dylan Tassé,[a] Victor Quezada-Novoa,[b] Christopher Copeman,[b] Ashlee J. Howarth,[b] and Alain Rochefort*[a]

The adsorption of CO_2 in MOF-808, NU-1000 and a series of rare-earth CU-10 analogues has been studied with first principles DFT and classical Monte-Carlo methods. DFT calculations describe the interaction of CO_2 with the different metal-organic frameworks (MOFs) as physisorption, but where we can distinguish several adsorption sites in the vicinity of the metal nodes. Beyond the identification of adsorption sites, the MOFs were synthesized, activated, and characterized to evaluate their experimental N_2 and CO_2 adsorption capacity. Classical Grand Canonical Monte-Carlo (GCMC) simulations for the adsorption of CO_2 are in very good agreement with DFT results for identifying the most favored adsorption sites in the MOFs. In contrast, a rather mixed agreement between GCMC simulations and experimental results is found for the estimation of adsorption capacity of several MOFs studied toward N_2 and CO_2.

Introduction

In the transition towards more sustainable energy, there is a growing demand for carbon-neutral fuels and chemicals.[1,2] Traditionally, fuels and chemicals have been produced through catalytic processes using petroleum-derived resources. However, transitioning to renewable hydrogen (H_2) and carbon sources can significantly mitigate greenhouse gas (GHG) emissions and facilitate the closure of carbon loops.[3,4] This shift is crucial for advancing towards a circular economy model.[5] Given the actual circumstances, Carbon Capture and Utilization (CCU) has garnered significant interest as a promising technical solution for both present and future energy systems.[6,7] An effective approach to carbon capture involves adsorption using solid materials, such as employing metal–organic frameworks (MOFs).[7,8] MOFs are composed of metal clusters interconnected by organic linkers to form a porous structure with significant surface area.[9,10] MOFs have been studied for many industrial applications because of their unique physical and chemical properties,[11,12] including gas storage,[13] gas purification,[14] gas separation,[13,14] catalysis[15] and many more. Some MOFs are quite chemically and thermally stable,[16] which is useful to convert CO_2 catalytically after capture. A number of MOFs have been synthesized and studied as candidates for CO_2 capture.[17] Some of them are Zr-based MOFs such as MOF-808[18,19] and NU-1000.[20,21] More recently, rare-earth (RE) metals like Y, Gd and Yb, have been introduced in MOFs with a **shp** topology and high porosity (RE-CU-10, RE = Y(III), Gd(III) and Yb(III); CU = Concordia University).[22,23]

In the present work, we have investigated the most relevant adsorption sites of CO_2 in different MOFs by first principles calculations (DFT), and we have calculated their uptake capacity with the help of classical Grand Canonical Monte-Carlo (GCMC) simulations. The results of the simulated adsorption isotherms were compared to the N_2 and CO_2 measurements carried out experimentally, at 77 K and 298 K, respectively, on freshly prepared MOFs. For this study, we considered MOF-808, NU-1000 and a series of RE-CU-10 analogues (RE = Y(III), Gd(III) and Yb(III)). MOF-808 consists of a network formed by 1,3,5-benzenetricarboxylic acid (H_3BTC) linkers and $[Zr_6O_4(OH)_4(HCOO)_6]^{6+}$ metal nodes.[18] NU-1000 is also a Zr-based MOF made from 1,3,6,8-tetrakis(*p*-benzoic acid) pyrene (H_4TBAPy) linkers and hexa-Zr metal nodes $[Zr_6O_4(OH)_8(H_2O)_4]^{8+}$.[20] RE-CU-10 has been recently synthesized[22,23] and is composed of 1,3,6,8-tetrakis(*p*-benzoic acid) pyrene (H_4TBAPy) linkers and nonanuclear RE(III)-cluster nodes. Three rare-earth metal nodes have been considered; yttrium (Y-CU-10), gadolinium (Gd-CU-10) and ytterbium (Yb-CU-10) $[RE_9(OH)_{12}(O)_2]^{11+}$ (RE = Y or Gd) and $[Yb_{11}(OH)_{18}(O)_2]^{11+}$. We analyzed the most favorable active sites through a comparison of adsorption energies of CO_2, the Bader charge distribution and the variation of CO_2 geometry. We conducted, in parallel, classical Monte-Carlo simulations to model the adsorption isotherms, yielding the CO_2 adsorption capacities for the MOFs considered. Our study supports the hypothesis of a relatively weak electrostatic interaction between CO_2 and the various MOFs studied. Furthermore, our classical GCMC simulations are in agreement with the relative stability of adsorption sites identified with DFT calculations, and provide adsorption capacities that compare well with our experimental data.

[a] *D. Tassé, Prof. A. Rochefort*
Department of Engineering Physics,
Polytechnique Montréal,
Montréal, (Québec) Canada
E-mail: alain.rochefort@polymtl.ca

[b] *V. Quezada-Novoa, C. Copeman, Prof. A. J. Howarth*
Department of Chemistry, Concordia University,
Montréal, (Québec) Canada

Supporting information for this article is available on the WWW under https://doi.org/10.1002/cphc.202401050

Computational Details

Density Functional Theory (DFT) calculations were performed at T = 0 K with the Siesta package[24] (v.4.1.5). Periodic boundary conditions have been applied for all the models using the exchange-correlation functional derived by Perdew, Burke, and Ernzerhof (PBE) within the generalized gradient approximation (GGA).[25] The semi-classical van der Waals corrections (D3) developed by Grimme[26] have been used. The PBE + D3 calculations used norm-conserving Trouillier-Martins pseudopotentials along with double-ζ polarized atomic basis sets. The DFT calculations employed a mesh cutoff of 300 Ry for constructing the real space grid. Structural relaxation were conducted using the conjugate-gradient method until the forces and the change in total energy were lower than 0.01 eV/Å and 0.0001 eV, respectively. The primitive unit cell was used for all MOF models, with the exception of MOF-808 which, according to a multi-scale modelling, truncated models were also considered for CO_2 adsorption calculations. Spin-polarized simulations were performed to take account of the magnetic character of RE atoms in the different RE-CU-10 systems. The adsorbed CO_2 was fully relaxed while the MOFs were maintained fixed at the optimized geometry for isolated crystal. All relaxation steps were carried at Γ-point using a *k*-point mesh of 1×1×1. Bader charge analysis was carried out using the code developed by the Henkelman group.[27] Adsorption energy of CO_2 was estimated as follows:

$$E_{ads} = E_{MOF} + E_{CO_2} - E_{CO_2/MOF} \quad (1)$$

where $E_{CO_2/MOF}$, E_{MOF}, and E_{CO_2} represent the total electronic energies calculated at 0 K for MOF + CO_2, and the isolated MOFs and CO_2, respectively. A more positive value of E_{ads} indicates a stronger bonding of CO_2 on the site.

Classical Grand Canonical Monte-Carlo (GCMC) simulations were carried out at T = 298 K with the RASPA 2.0 package[28] using the periodic geometries obtained from DFT calculations to obtain details on the adsorption process and to determine the adsorption capacity of the MOFs. The CO_2 molecule was modelled using the TraPPE force field[29] and all the fixed MOFs models were described by a combination of Universal Force Field (UFF)[30] and DREIDING force field.[31] The Lennard-Jones parameters between distinct atoms (see Table S1, SI) were computed using the Lorentz-Berthelot mixing rule. Lennard-Jones interactions were determined by imposing a spherical cut-off of 12 Å, and incorporating long-range corrections. Long-range electrostatic interactions were assessed via Ewald summation.[32] Partial atomic charges for MOF atoms were derived using the charge equilibration method (Q_{eq}).[33,34] Convergence for the adsorption isotherms was achieved through 75,000 GCMC cycles, consisting of an initial 25,000 cycles designated for equilibrium and a subsequent 50,000 cycles for ensemble averages. The density distribution of adsorbed CO_2 in the different MOFs were visualized using the software iRASPA.[35] The pressure was converted to fugacity using the Peng-Robinson equation of state. The critical temperature, the critical pressure and the acentric factor used for the CO_2 simulations are : 304.1282 K, 7377300.0 Pa and 0.22394. Within the low-pressure range of 0–1 bar considered in our numerical-experimental comparisons, gas pressure and fugacity are nearly identical.

Experimental Details

Synthesis of MOF-808

MOF-808 was synthesized using a scaled-up procedure[36] by combining 9.7 g of $ZrOCl_2 \cdot 8H_2O$ with 6.3 g of H_3BTC in 750 mL each of DMF and formic acid in a 2 L screw-top jar, with the lid loosely attached to allow for pressure release. The resulting mixture was sonicated until all components dissolved and then placed in an oven at 120 °C to react for 72 hours. The MOF was collected via vacuum filtration and washed three times with fresh DMF (3 × 400 mL), soaked in fresh DMF (400 mL) overnight, followed by three acetone washes (3 × 400 mL), and soaked in acetone (400 mL) overnight. Finally, the material was dried in a vacuum oven at 80 °C for one hour and then activated on a Micromeritics SmartVacPrep at 120 °C for 20 hours.

Synthesis of NU-1000

NU-1000 was synthesized on a 200 mg scale using the reported procedure,[37] combining 388 mg of $ZrOCl_2 \cdot 8H_2O$ and 10.8 g of benzoic acid in 32 mL of DMF in a 100 mL screw-top jar, followed by sonication until fully dissolved. The mixture was placed in an oven for 1 hour at 80 °C. After cooling, 160 mg of H_4TBAPy was added, and the solution was sonicated for 20 minutes before being placed in the oven for 15.5 hours at 100 °C. The MOF was collected via centrifugation and washed three times with fresh DMF (3 × 45 mL), followed by soaking in fresh DMF overnight (45 mL). The product was then placed in a 100 mL screw-top jar with 52 mL of DMF and 2 mL of 8 M HCl, and heated in an oven for 12 hours at 100 °C. Subsequently, the MOF was washed three times with DMF (3 × 45 mL) and soaked in fresh DMF overnight, followed by three 12-hour acetone washes (3 × 45 mL). Finally, the material was dried in a vacuum oven at 80° C for one hour and then activated on a Micromeritics SmartVacPrep at 120° C for 20 hours.

Synthesis of Y-CU-10

In a 250 mL Pyrex jar, 99.0 mg of H_4TBAPy (0.145 mmol), 227.0 mg of $Y(NO_3)_3$ hydrate (0.0581 mmol, assuming hexahydrate), and 9151.9 mg of 2-fluorobenzoic acid (65.3 mmol) were mixed with 51 mL of DMF. The suspension was sonicated to obtain a homogeneous solution, followed by the addition of 11.6 mL of glacial acetic acid (0.203 mol) and 1000 μL of Milli-Q water (58.1 mmol). The suspension was sonicated for 5 minutes and then placed in a convection oven at 120° C for 72 hours. The material was activated at 120° C for 24 hours. Yield: 112.6 mg, 23 %.

Synthesis of Gd-CU-10

In an 8-dram vial, 51.0 mg of H_4TBAPy (0.0227 mmol), 103.4 mg of $Gd(NO_3)_3$ hydrate (0.0227 mmol, assuming hexahydrate), and 3074.3 mg of 2-fluorobenzoic acid (21.9 mmol) were mixed with 15 mL of DMF. The suspension was sonicated until a homogeneous solution was obtained, then placed in a convection oven at 120° C for 72 hours. The material was activated at 120° C for 24 hours. Yield: 76.7 mg, 25 %.

Synthesis of Yb-CU-10

In a 250 mL Pyrex jar, 51.4 mg of H_4TBAPy (0.0754 mmol), 176.9 mg of $Yb(NO_3)_3$ hydrate (0.0384 mmol, assuming pentahydrate), and 5296.5 mg of 2-fluorobenzoic acid (37.7 mmol) were mixed with 29 mL of DMF. The suspension was sonicated to obtain a homogeneous solution, followed by the addition of 339 μL of Milli-Q water (18.8 mmol) and 462 μL of concentrated (68 %) nitric acid (7.54 mmol). The suspension was sonicated for 5 minutes and then placed in a convection oven at 120° C for 72 hours. The material was activated at 120°C for 24 hours. Yield: 85.3 mg, 25 %.

Characterization

Powder X-ray diffraction (PXRD) patterns were collected on a Rigaku Miniflex 6G equipped with a Cu-target ($\lambda = 1.54$ Å) sealed-tube X-ray source operating at 40 kV/15 mA and a D/teX Ultra detector over a range of $3 < 2\theta < 40^{\circ}$ at a scan rate of 10° per minute. PXRD patterns are shown in SI (see Figure S1-S3).

MOF samples were activated using a Micromeritics SmartVacPrep instrument equipped with a hybrid turbo vacuum pump. Carbon dioxide adsorption isotherms were measured at 298 K on a Micromeritics 3Flex instrument. Nitrogen (N_2) adsorption-desorption isotherms were measured at 77 K on a Micromeritics TriStar II Plus instrument. Brunauer-Emmett-Teller (BET) surface areas are calculated using isotherm points between 0.0005 and 0.1 P/P_0 that satisfy all BET criteria. The comparison of experimental and theoretical N_2 adsorption isotherms for RE-CU-10 are reported in Figure S4, while Figure S5 shows MOF-808 and NU-1000 results in comparison to previous experimental data.[38] Figure S5 confirms that GCMC can correctly reproduce our and previous experimental results for MOF-808, but it emphasizes the large variations observed for NU-1000. For this system, we have measured a lower saturation uptake while we have calculated a higher uptake by nearly the same amount with respect to previous experimental results (lines with circles). Nevertheless, the general shape of the experimental curves are correctly reproduced by GCMC, then the discrepancies could be attributed to a difference in the volume probed by N_2, most probably due to structural and chemical defects.

Results and Discussion

Structural Properties of MOFs

Several metal-organic framework models have been considered in the present study. First, MOF-808[18] is a well-known and studied material for CO_2 adsorption.[19,39–41] As given its complex structure, a multi-scale analysis has been performed of this MOF to determine the influence of the chemical environment around a given site on its adsorption properties. This analysis will be discussed in the next section. MOF-808 consists of an octahedral Zr_6 cluster bridged by four μ_3-O and four μ_3-OH ligands (see Figure S6, SI). Each node is connected to six BTC linkers (see Figure S7, SI), while the remaining Zr coordination sites are capped by six formate ligands. MOF-808 exhibits a three-dimensional framework characterized by a 3,6-connected structure, showcasing a **spn** framework topology. The different models considered for the multi-scale DFT simulations are (i) MOF-808-node1, with a single metal cluster alongside 6 formate ligands and 6 BTC linkers; (ii) MOF-808-node2, with two metal clusters with 9 BTC linkers and 12 formate ligands; and (iii) the full unit cell of MOF-808. Those different models are shown in Figure 1. The porous system of MOF-808 consists of two micropores with pore-diameter of $\phi = 18.4$ Å and $\phi \leq 10$ Å.[18,42,43]

A second very well known MOF is NU-1000.[20,44] This MOF is composed of a similar octahedral Zr_6-cluster as for MOF-808 (see Figure S6, SI). Among the 12 octahedral edges, 8 are connected to tetratopic H_4TBAPy units (see Figure S7, SI), while the remaining Zr coordination sites are occupied by terminal

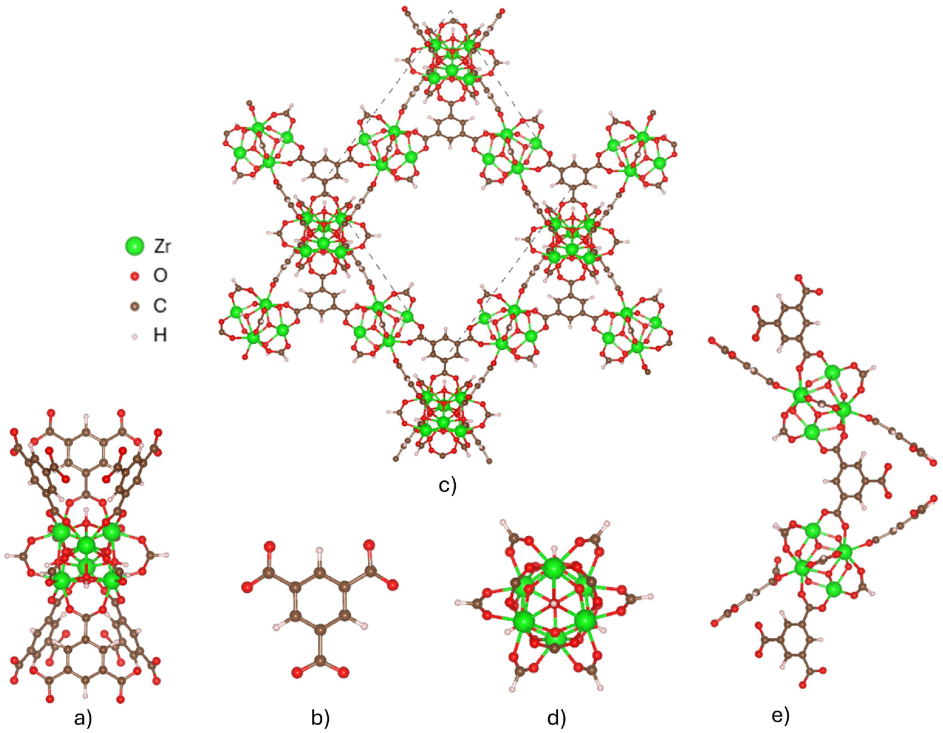

Figure 1. MOF-808 structure representing a **spn** topology a) MOF-808-node1 model, b) BTC linker, c) MOF-808 unit cell, d) Zr-node with formate capping ligand, and e) MOF-808-node2 model.

-OH, terminal -OH_2 and bridging μ_3-O and μ_3-OH ligands. The 3D structure can be characterized as 2D Kagome sheets linked by H_4TBAPy ligands. NU-1000 is characterized by a **csq** topology. DFT calculations and GCMC simulations were conducted using the complete NU-1000 unit cell illustrated at Figure 2. This MOF has mesopores with diameters of 30 Å and micropores of 12 Å.[20,45]

Finally, for the RE-CU-10 MOF series, the periodic models have been taken from the Cambridge Structural Database (CSD)[46] and described as reported in the literature.[23] Y-CU-10 and Gd-CU-10 have a similar structure, where only the metal node is different because of the rare-earth metal (see Figure S8, SI). The nodes consist of 9 metals atoms with bridging μ_3-OH and μ_3-O ligands interconnected with 4 tetratopic linkers H_4TBAPy. Yb-CU-10 is slightly different with 11 metal atoms and 18 bridging μ_3-OH and 2 bridging μ_3-O (see Figure S9, SI). RE-CU-10 corresponds to an **shp** topology. For both DFT and GCMC simulations, the periodic structure has been used since it consists of only one node that is repeated periodically. The unit cells for the RE-CU-10 are shown in Figure 3. Each MOF exhibits closely resembling lattice parameters: Y-CU-10 has $a = b =$ 22.16 Å and $c = 16.37$ Å, Gd-CU-10 features $a = b = 22.04$ Å and $c = 16.91$ Å, while Yb-CU-10 has $a = b = 21.92$ Å and $c = 16.55$ Å. The calculated pore size distributions closely match the experimental values[22,23] with a pore diameter of 11 Å.

Identification of Adsorption Sites

To explore all possible adsorption sites in complex porous systems, DFT techniques are not considered the most practical tool. We have focused our attention on three highly probable adsorption sites for each MOF. For the Zr-based MOFs, MOF-808 and NU-1000, the most active sites are located in the vicinity of the Zr_6 node within the mesopore and micropore. Although MOF-808 and NU-1000 were partially investigated with DFT,[42,47] there are no reported works using DFT or GCMC techniques for the RE-CU-10 systems. Then, we have investigated the RE-based MOFs by examining CO_2 adsorption on noteworthy metal sites located within the pores, and nearby the linkers. To this end, we performed DFT calculations on the pristine crystal to characterize their electronic properties through the electrostatic potential and the charge density distribution. This approach allowed us to identify the regions where CO_2 could more probably adsorb.

The adsorption of CO_2 is generally considered a local process, so we have first truncated the unit cell of MOF-808 to simplify the analysis of bonding, to evaluate the impact of a more explicit model, and more importantly to attempt reducing the computational time. The different truncated models shown in Figure 1, represent one-node, two-nodes and a full periodic structure of MOF-808. Three adsorption sites have been probed with CO_2: the *Core* site (near the Zr core), the *Interface* site (at the junction between two BTC^{3-} linkers), and the *Minipore* site (within the small pore), as illustrated in Figure 4. Although the relative stability of these sites will be discussed below, we choose the *Core* site that is located in the mesopore to compare the truncated models. In addition, we have tested different functional PBE(PBE + D3, PBE + D3 + U) and vdW (LMKLL) to validate our DFT approach, the results are reported in Table 1.

According to Table 1, the most obvious variations in adsorption energy occurs when we include the dispersion energy. The adsorption energy increases similarly from simple PBE functional to the different functionals that take dispersion energy into account (PBE + D3, PBE + D3 + U*, vdW). Moreover, the different truncated models show very similar adsorption energy and lead to a quite small charge transfer from the MOF to the CO_2 moiety. The magnitude of adsorption energy of ~1 eV is representative of the relatively weak electrostatic interaction of CO_2 with the MOF in physisorption. This is also supported by the weak charge transfer toward CO_2 calculated at PBE + D3 level. This indicates that CO_2 is primarily physisorbed, and that van der Waals interactions dominate. This result shows that a small model like MOF-808-node1 is large

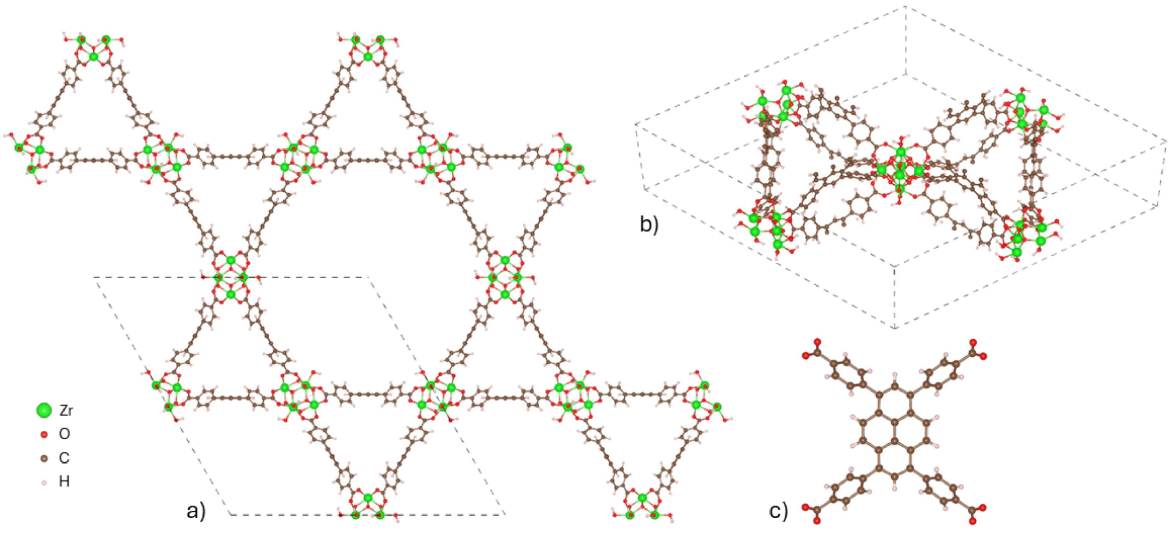

Figure 2. a) NU-1000 structure representing a **csq** topology b) a side view of the NU-1000 unit cell, c) H_4TBAPy linker.

Research Article
doi.org/10.1002/cphc.202401050
Chemistry Europe
European Chemical Societies Publishing

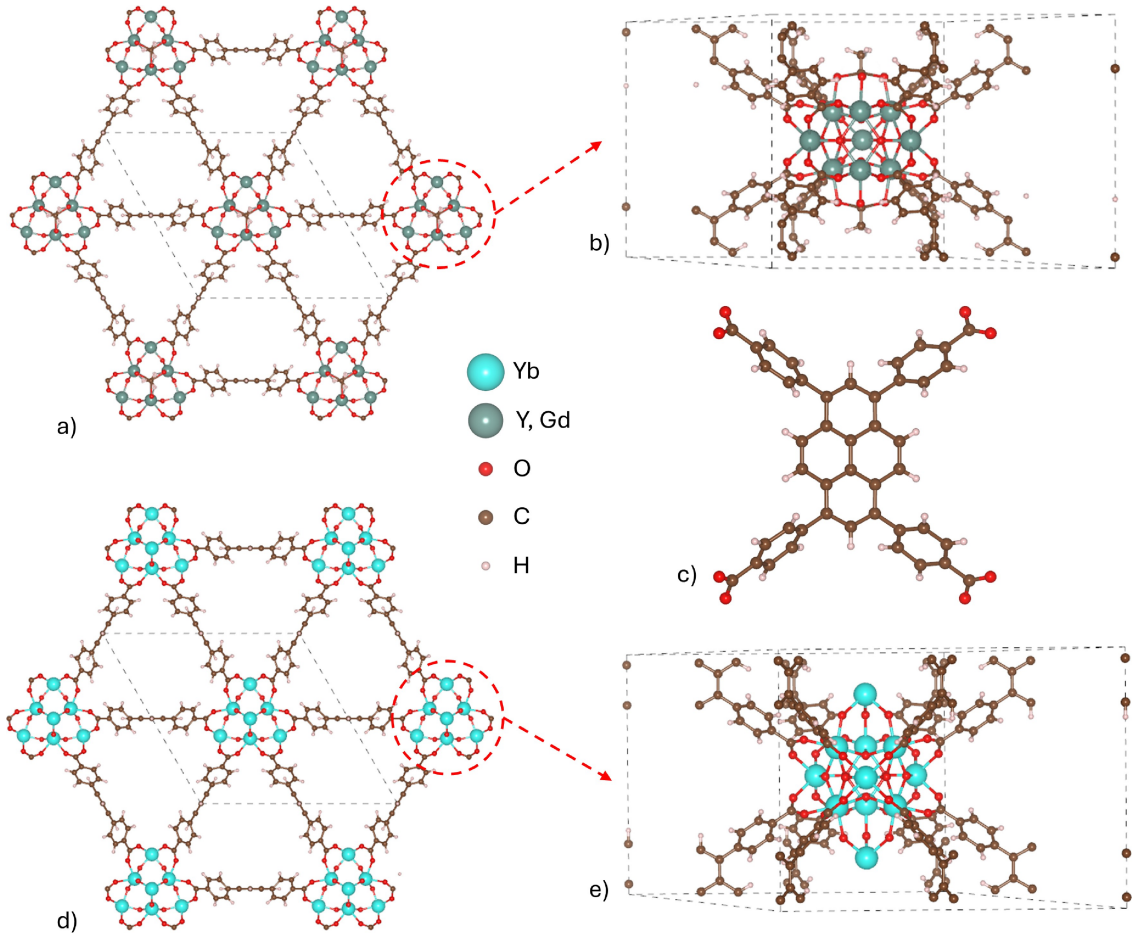

Figure 3. RE-CU-10 structure : representing an **shp** topology a) RE_9-CU-10, b) Unit cell of Y/Gd-CU-10, c) H_4TBAPy linker, d) RE_{11}-CU-10, e) Unit cell of Yb-CU-10.

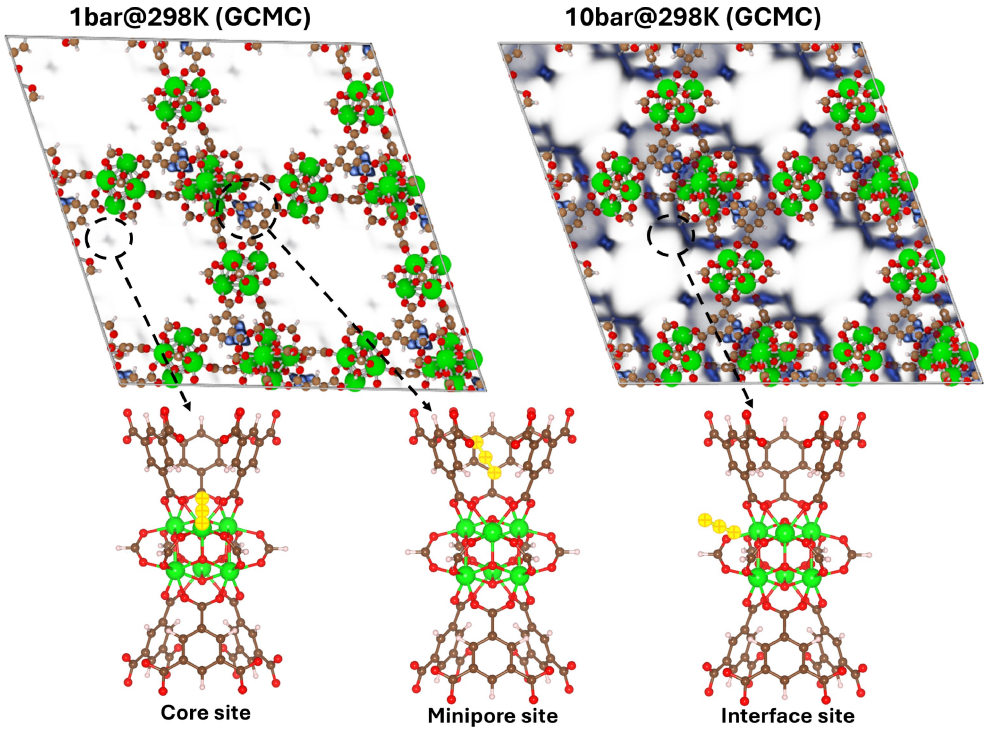

Figure 4. CO_2 concentration distribution within MOF-808 at 1 and 10 bar at 298 K. The adsorption sites considered in the DFT calculations are also identified.

Table 1. Comparison of adsorption energy (E_{ads}, in eV) and Bader charge distribution (Q_B) of CO_2 adsorbed on a *Core* site in MOF-808 models using different DFT functionals.

Models	PBE	PBE + D3	PBE + D3 + U*	vdW	$Q_B(CO_2)$ (|e|)
MOF-808-node1	0.73	0.95	0.97	0.98	−0.0123
MOF-808-node2	0.74	0.96	0.97	0.98	−0.0085
MOF-808-periodic	0.75	0.99	1.00	1.01	−0.0064

*$(U - J) = 4$ eV on Zr metal atom.

enough to reproduce the main features of CO_2 adsorption, at least at the single molecule level. The DFT + U calculations where $U - J = 4$ eV correction was applied to the Zr metal atom in agreement with previous work,[48] that correlation energy does not play a major role on the adsorption energy, nor on the electronic properties of MOF-808. Hence, DFT calculations at the PBE + D3 level give a representative description of the adsorption process, even on a highly truncated model.

Following this PBE + D3 approach, we have evaluated the adsorption energy, the Bader charge distribution and the structural properties of CO_2 on the different adsorption sites reported in Table 2. Although individual results will be discussed in more details below, we emphasize that CO_2 remains physisorbed on every adsorption site of the MOFs studied. This observation is supported by the calculated charge transfer and the variation of geometry observed for CO_2. In addition to the DFT calculations, we used classical Grand Canonical Monte Carlo (GCMC) simulations to estimate the variation of CO_2 concentration among the pores of the different systems. With GCMC simulations, we can identify the zone of interest for CO_2 adsorption at different pressures at room temperature, and compare them to the relative stability of adsorption sites found with high level DFT calculations performed at 0 K. The distribution of CO_2 among the MOFs was plotted as a function of pressure to monitor the saturation of active sites. In contrast to DFT calculations in which we focus on the interaction of a single CO_2 molecule with an active site, classical GCMC simulations involve a large amount of CO_2 molecules. In this case, truncated models are not suitable to represent the chemical environment of a pore where it becomes crucial to correctly describe CO_2-MOF and CO_2-CO_2 interactions. For that reason, classical GCMC simulations are performed on full unit cell of MOFs.

Along with the DFT results for the adsorption of CO_2 on the three sites considered for MOF-808-node1 model in Table 2, the GCMC results obtained on a full MOF-808 unit cell are summarized in Figure 4. Dark blue areas indicate regions of higher CO_2 concentration. The nature and position of the most active adsorption sites of MOF-808 can be easily identified in Figure 4. In general, the DFT results agree very well with the trend observed from GCMC simulations. At 1 bar, both *Core* and

Table 2. Adsorption energy (E_{ads}), Bader charge (Q_B), and structural properties (∠ : O–C-O angle; d(CO_2-MOF) : shortest distance between CO_2 and MOF) of CO_2 on MOF systems.

MOF	Site	E_{ads}	$Q_B(CO_2)$	$\angle CO_2$	d(CO_2-MOF)
		(eV)	**(|e|)**	**(°)**	**(Å)**
	Core	0.95	−0.0121	178.6	2.75
MOF-808	Minipore	1.36	−0.0165	179.5	2.70
	Interface	0.92	−0.0175	174.7	2.70
	Site 1	1.06	−0.0299	179.4	3.02
NU-1000	Site 4	1.07	−0.0100	178.0	3.15
	Site 5	1.10	−0.0010	178.5	2.90
	Hole	0.92	−0.0150	178.1	3.82
Y-CU-10	Peak	1.03	−0.0160	179.5	3.48
	Linker	0.76	−0.0310	179.5	3.03
	Hole	1.15	−0.0200	178.8	3.60
Gd-CU-10	Peak	1.23	−0.0160	179.1	3.33
	Linker	1.04	−0.0220	178.7	2.89
	Hole	0.98	−0.0190	180.0	3.40
Yb-CU-10	Peak	1.17	−0.0150	180.0	2.67
	Linker	0.78	−0.0310	179.5	3.10

Minipore sites are clearly occupied. These two sites are the most stable conformations found with DFT (see Table 2). As the pressure increases, the presence of CO_2 at the *Interface* site becomes more prominent, indicating the onset of site saturation. Furthermore, at 10 bar, the CO_2 concentration in the *Minipore* remains unchanged, suggesting that this site is already saturated at low pressure. It is interesting to note that the *Minipore* site is the more stable adsorption site considered, but becomes rapidly saturated due to the very limited volume available in this small micropore (diameter ~4.8 Å) to store CO_2. Moreover, due to its position, we can anticipate that an adsorption on this site will be quite limited due a lower accessibility with respect to the sites located in the larger pore.

For NU-1000, Table 2 shows that the three adsorption sites studied present quite similar properties, and Figure S10 (see SI) reveals that these sites are fully accessible at low pressure and room temperature. This last trend is not so surprising because NU-1000 is highly porous, and its open pores can be easily occupied. For the RE-CU-10 series, three adsorption sites around the **shp** topology were compared. As mentioned above, the identification of active sites in RE-CU-10 was mostly based on the analysis of the electrostatic potential mapping. A comparison of electrostatic potential for Y, Gd, Yb-CU-10 shows that the active sites should be essentially located in the vicinity of the metal node (see Figure S11, SI). All three identified active sites (*Hole, Peak, Linker*) and the CO_2 concentration are reported in Figure 5 for Y-CU-10. A similar trend was observed for the other MOFs, and the CO_2 concentration distributions for Gd- and Yb-CU-10 are given in Figure S12. Based on adsorption energy, Gd-CU-10 appears to interact more strongly with CO_2, a relatively high adsorption energy of 1.23 eV was calculated for the *Peak* site. This adsorption site was also found to be the most stable in the other RE-CU-10 analogues, while the *Linker* site is systematically less stable. As described for MOF-808, the adsorption energy and Bader charge distribution agree to describe the interaction between CO_2 and different MOFs as physisorption, dominated by weak electrostatic interactions. The GCMC results agree well with the DFT results. At 1 bar, both *Hole* and *Peak* sites are occupied, although the concentration of CO_2 at the *Peak* site is less pronounced at low pressure suggesting a slow CO_2 adsorption saturation. At 10 bar, there is a high concentration of CO_2 near the center of the pore which suggests a good affinity between the H_4TBAPy linker and CO_2 molecule. This site corresponds to the *Linker* site reported in Table 2.

CO_2 Adsorption Capacity

To complete our analysis of CO_2 adsorption in these select cluster-based MOFs, we used the GCMC approach to estimate their adsorption capacity at room temperature and compare them with our experimental data. The experimental isotherms were measured at room temperature (298 K), ranging from 0 to 1000 mbar. GCMC simulations were performed over higher pressure range (0-15 bars) to estimate the overall CO_2 saturation capacity. Beyond GCMC used to estimate CO_2 uptakes, we also carried out DFT calculations using Y-CU-10 to determine the number of CO_2 molecules that can fit in a given pore. To this end, we added one CO_2 molecule at a time into

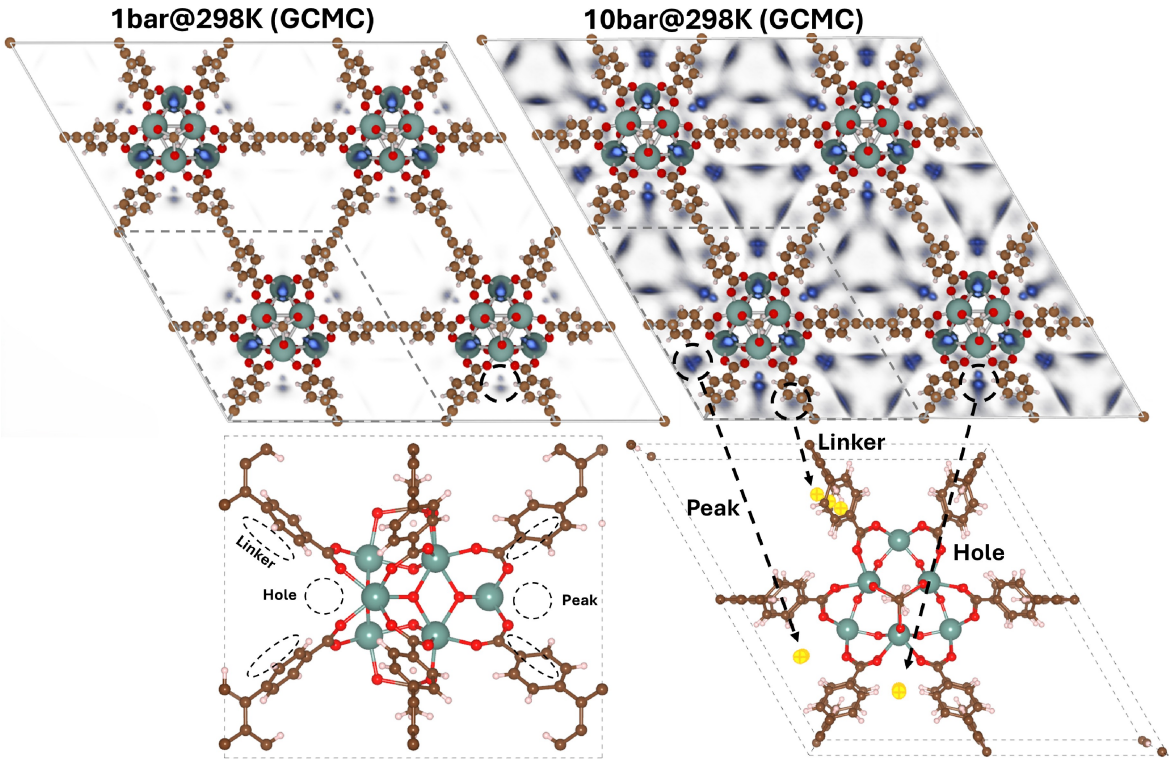

Figure 5. Distribution of CO_2 concentration within Y-CU-10 at 1 bar and 10 bar at 298 K and the corresponding adsorption sites

the pore to follow the variation of adsorption energy along the molecule addition process.

We need to stress that in GCMC simulations, the position in space where CO_2 is added/removed is randomly chosen, and considered all empty space within the MOF. This is in contrast with experiments in which CO_2 has to diffuse among the porous media to reach an adsorption site, and in this case the adsorption process may be limited by the diffusion of the molecule. In order to probe the entire porous volume of the MOF, one usually has to increase the CO_2 pressure. For the MOFs studied, the behaviour of CO_2 adsorption at higher pressure can be associated to a Dubinin-Astakhob type,[49] where the capacity of the RE-CU-10 series dominate (see Figure S13, SI). A relevant approach to compare GCMC simulations to experimental results is to compare the CO_2 uptake for a comparable accessible volume. In this case, the crystal density or the skeletal density can be used to convert gravimetric data into volumetric data. Considering that we used pressures below 1 bar, such converted CO_2 uptake should be more representative of the experimental conditions where the MOF contains a significant amount of weakly accessible pore volume. We have determined the skeletal density for the RE-CU-10 series with helium pycnometry, they are compared in Table S3 to the crystal densities that were estimated from single crystal XRD.

Figure 6 compares the calculated volumetric CO_2 uptake (cm^3/cm^3) isotherms to experimental data for the different MOFs using the crystal density. We found a reasonable agreement between experimental data and GCMC simulations for NU-1000, but the calculated CO_2 uptake is systematically overestimated for the RE-CU-10 series, and it is clearly underestimated for MOF-808 (see also Table S4, SI). Nevertheless, the overestimations for the RE-CU-10 series are significantly reduced when the uptakes are determined with the skeletal density (see Figure S14, SI), suggesting that such MOFs contain a significant amount of inaccessible pores. Furthermore, considering the uncertainties in the measurement of CO_2 uptakes for the RE-CU-10 series (see Figure S15, SI), the agreement between experimental and GCMC data becomes significantly improved. Surprisingly, the trend observed for the adsorption of CO_2 in MOF-808 and NU-1000 is completely opposed to N_2 where GCMC simulations gave reasonable agreement to experiments for MOF-808 but not for NU-1000. Although we do not have a clear explanation for this contrasting behavior for these two MOFs with respect to N_2 or CO_2, a more systematic study on the parametrization of Lennard-Jones parameters would be necessary for identifying the source of the deviations.

We have previously compared the adsorption of N_2 in MOF-808 and NU-1000 (Figure S5, SI), and we can also compare our experimental and theoretical results to previous results for the case of CO_2. For NU-1000, the agreement between our results and previous results is relatively satisfying; we are slightly underestimating the CO_2 uptakes (see Figure S16, SI). According to the fact that a larger volume in MOF is usually probed within a GCMC simulation, we may anticipate that the uptakes will be also overestimated in GCMC. This contrasts strongly with the results obtained for MOF-808 where the calculated CO_2 uptake

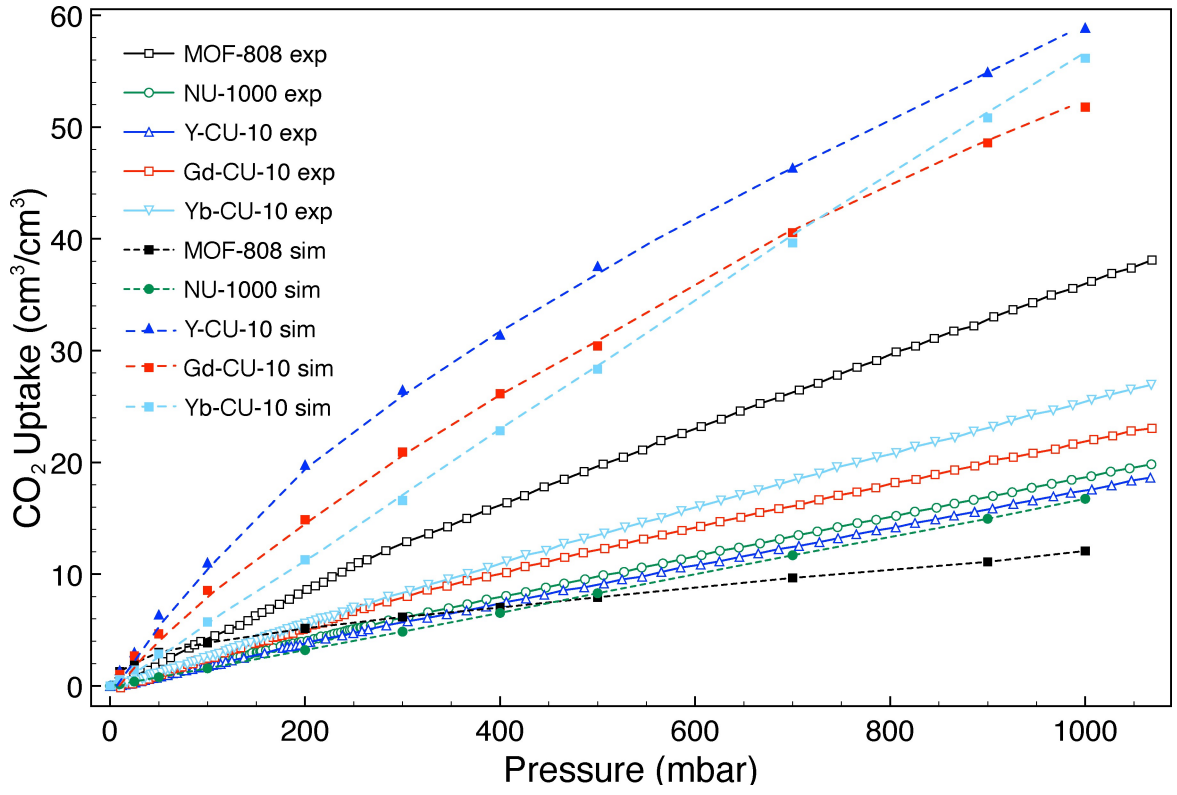

Figure 6. Comparison of the simulated isotherm of CO_2 in volumetric units (cm^3/cm^3) with experimental data from 0 to 1 bar at 298 K for MOF-808, NU-1000, Y-CU-10, Gd-CU-10 and Yb-CU-10. (opened symbols are from experiments, filled symbols are from GCMC simulations). Crystal density was used to convert gravimetric units to volumetric units.

is radically underestimated. This is an apparent behaviour that was previously observed, and was partly attributed to the dynamic nature of the capping ligands on the MOF-808 node.[42] Hence, the nature of the static capping ligands (formate, -OH, -OH_2, etc.) in the sample could have a drastic influence on the adsorption capacity of MOF-808. However, such explanation is not sufficient to relate the quite large discrepancy between experimental and theoretical CO_2 uptakes. As revealed in Figure S17, previous GCMC simulations[42] are also largely underestimating the CO_2 uptake (blue dashed line), and although removing the capping ligands around the metal core (blue dotted line) reduces the uptake difference, the general shape of the curve is drastically different to experimental results. Hence, our results are consistent with previous theoretical results but all the GCMC simulations show a clear weakness in reproducing the experimental results. In general, the discrepancies of GCMC simulations from experimental data may be attributed to factors such as defects, disorder, activation conditions or more subtle molecular interactions that are not taken into account such as charge transfer, quantum size effects, etc. For example, the capping ligand in RE-CU-10 is not totally well characterized experimentally,[23] and its chemical reactivity may not be correctly described in GCMC simulations. Although we have clearly identify different adsorption sites with the help of DFT and GCMC simulations, we need to improve our understanding of the influence of capping ligands on the adsorption capacity of MOFs in a further study.

To validate the uptake obtained from GCMC simulation, and estimate the number of CO_2 molecules that can stand in a micropore, we performed DFT calculations on the systematic adsorption of CO_2 in a pore of Y-CU-10. By incrementally adding CO_2 molecules, we follow the variation of adsorption energy to better identify the different steps involved in the adsorption process. A plateau in the adsorption energy curve indicates that the additional CO_2 molecules compete with each other to adsorb (or condense) on similar sites. We need to emphasize that our one-by-one approach is one specific representation of the pore filling process, a more rigorous approach would have necessitated a multiconfiguration representation of CO_2 molecules within the pore. Although a multiconfiguration approach was not realistic using DFT, we considered in our calculations that every time a CO_2 was added to the pore, the total number of CO_2 molecules were fully relaxed within the MOF. Hence, every step in this one-by-one process leads to a stable CO_2 distribution, where CO_2-CO_2 repulsion is minimized. Due to a larger amount of CO_2 molecules contributing to the adsorption energy, this quantity was calculated as follow

$$E_{ads} = \frac{E_{MOF} + E_{CO_2}^{cluster} - E_{MOF/CO_2}}{N} \quad (2)$$

where E_{MOF/CO_2} represents the total energy of the entire MOF + CO_2 system, E_{MOF} is the total energy of pristine MOF, and $E_{CO_2}^{cluster}$ is the total energy of adsorbed CO_2 configuration without the MOF, N is the number of CO_2 molecules in the MOF. Such formulation accounts for intermolecular interactions between CO_2 molecules in the calculation of adsorption energy.

Figure 7 summarizes the calculated adsorption energy per CO_2 molecule after adding CO_2 one-by-one in the pore, followed by the relaxation of the entire number of CO_2 molecules. This figure clearly highlights the rapid saturation of the *Hole* site, as evidenced by the initial addition steps from 1 to 3 CO_2 molecules located near that site. Adsorption energies start at 0.92 eV, as reported in Table 2. As the number of CO_2

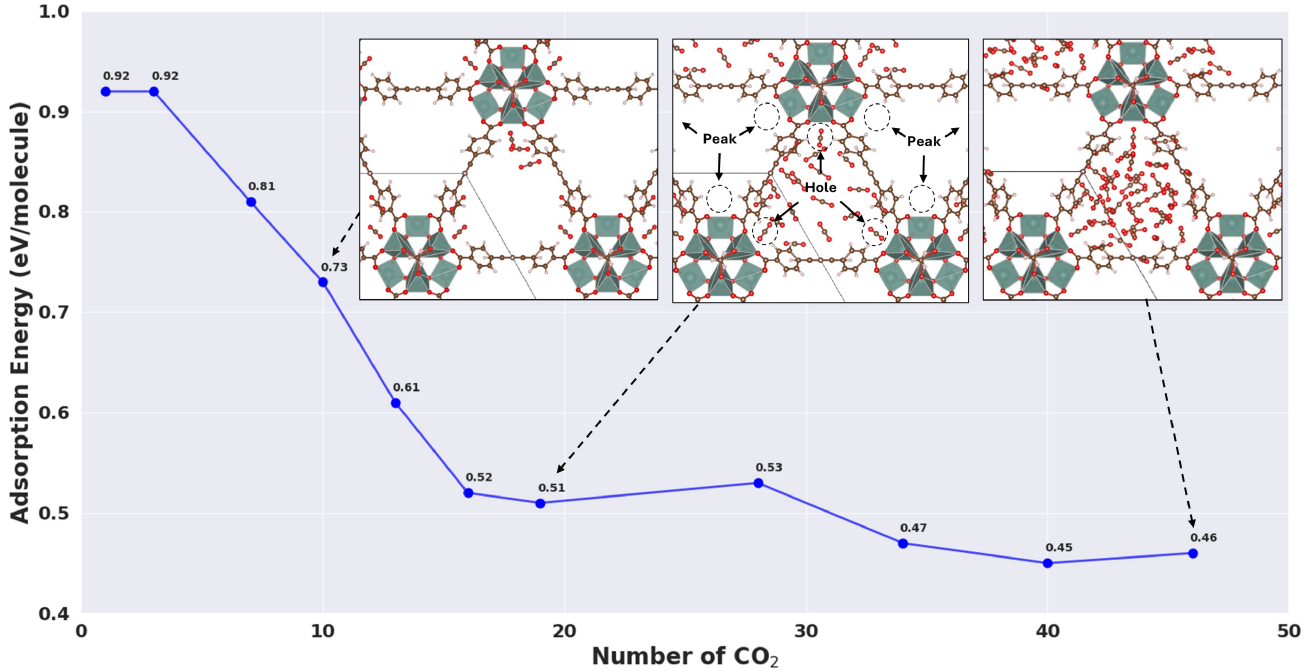

Figure 7. Variation of adsorption energy as a function of CO_2 concentration in a Y-CU-10 micropore. Snapshots of the CO_2 configuration at different stages of the pore filling are provided as insets.

molecules increases, the adsorption energy decreases; additional molecules occupy progressively less favorable sites. When the number of CO_2 molecules reaches $N=16$, the adsorption energy almost reaches a second plateau that indicates that *Linker* sites become saturated. The adsorption energy at that second plateau (~0.52 eV) is lower than the calculated values in Table 2 for *Linker* site due to CO_2-CO_2 interaction that globally contribute to decrease the adsorption energy. After $N=27$ molecules, the adsorption energy decreases slowly to reach a last plateau from $N=38$, with an adsorption energy of around 0.45 eV. At this point, we can consider that additional CO_2 molecules introduced in the MOF are not physisorbed on the Y-CU-10 surface but more simply, weakly interacting with other CO_2 molecules in a condensed phase. We recall that DFT calculations are performed at T = 0 K. Since a CO_2 condensed phase can only be observed below 195 K, we can estimate that less than 16 CO_2 molecules can stand in this micropore in atmospheric environment, that is when adsorption sites on Y-CU-10 are saturated. This quantity is similar to the number of CO_2 molecules calculated with GCMC at 298 K and 1 bar. To determine the maximum number of CO_2 molecules that can theoretically occupy this pore, we can approximate the pore as a sphere with a radius of 8 Å, and use the CO_2 density in solid state (1.76 g/cm^3);[50] a maximum number of 51 CO_2 molecules can occupy the empty space of that pore. Obviously, an adsorption at much lower temperature and higher pressure than atmospheric conditions is mandatory to reach such capacity experimentally.

Conclusions

Five different MOFs were studied using DFT and GCMC calculations : MOF-808, NU-1000, RE-CU-10 (RE = Y(III), Gd(III), Yb(III)). DFT calculations were carried out to evaluate the most favorable adsorption sites within the different models, and GCMC simulations to estimate their corresponding adsorption capacity at low pressure and ambient temperature. The GCMC simulations of N_2 and CO_2 adsorption were then compared to the experimental results obtained on the synthetized MOFs. According to DFT calculations, CO_2 molecules are physisorbed on the surface of all MOFs considered. For the case of MOF-808, a multi-scale modelling allowed us to show that a truncated one-node model is sufficient to catch the single CO_2 molecule interaction, and to evaluate its adsorption energy. In addition, we found a good agreement between GCMC simulations and DFT results for identifying adsorption sites but a rather mixed agreement between GCMC and experiments in the determination of the CO_2 and N_2 uptakes.

Acknowledgements

We acknowledge the financial support from FRQNT and NSERC through a NOVA grant. D.T. thanks Hydro-Québec for scholarship through the Institut de l'Énergie Trottier scholarship program. This work would have not been possible without the computational resources provided by Calcul Québec and the Digital Research Alliance of Canada (The Alliance).

Conflict of Interests

The authors declare no conflict of interest.

Data Availability Statement

The data that support the findings of this study are available from the corresponding author upon reasonable request.

Keywords: DFT · GCMC · CO_2 adsorption · MOF · isotherms

[1] K. Bourzac, *Nature* **2017**, *550*, S66.
[2] C. Hepburn, E. Adlen, J. Beddington, E. A. Carter, S. Fuss, N. Mac Dowell, J. C. Minx, P. Smith, C. K. Williams, *Nature* **2019**, *575*, 87.
[3] M. Bui, C. S. Adjiman, A. Bardow, E. J. Anthony, A. Boston, S. Brown, P. S. Fennell, S. Fuss, A. Galindo, L. A. Hackett, J. P. Hallett, H. J. Herzog, G. Jackson, J. Kemper, S. Krevor, G. C. Maitland, M. Matuszewski, I. S. Metcalfe, C. Petit, G. Puxty, J. Reimer, D. M. Reiner, E. S. Rubin, S. A. Scott, N. Shah, B. Smit, J. P. M. Trusler, P. Webley, J. Wilcox, N. Mac Dowell, *Energy Environ. Sci.* **2018**, *11*, 1062.
[4] A. Goeppert, M. Czaun, J.-P. Jones, G. K. Surya Prakash, G. A. Olah, *Chem. Soc. Rev.* **2014**, *43*, 7995.
[5] I. Tebbiche, J. Mocellin, L. T. Huong, L.-C. Pasquier, *27 - Circular Economy and Carbon Capture, Utilization, and Storage*, Elsevier **2021**.
[6] F. M. Baena-Moreno, M. Rodriguez-Galan, F. Vega, B. Alonso-Farinas, L. F. Vilches Arenas, B. Navarrete, *Energy Sources Part A* **2019**, *41*, 1403.
[7] A. Al-Mamoori, A. Krishnamurthy, A. A. Rownaghi, F. Rezaei, *Energy Technol.* **2017**, *5*, 834.
[8] M. Ding, R. W. Flaig, H.-L. Jiang, O. M. Yaghi, *Chem. Soc. Rev.* **2019**, *48*.
[9] H.-C. Zhou, J. R. Long, O. M. Yaghi, *Chem. Rev.* **2012**, *112*, 673.
[10] Q.-L. Zhu, Q. Xu, *Chem. Soc. Rev.* **2014**, *43*.
[11] H. Furukawa, K. E. Cordova, M. O'Keeffe, O. M. Yaghi, *Science* **2013**, *341*, 1230444.
[12] A. U. Czaja, N. Trukhan, U. Müller, *Chem. Soc. Rev.* **2009**, *38*.
[13] H. Li, K. Wang, Y. Sun, C. T. Lollar, J. Li, H.-C. Zhou, *Mater. Today* **2018**, *21*, 108.
[14] R.-B. Lin, S. Xiang, H. Xing, W. Zhou, B. Chen, *Coord. Chem. Rev.* **2019**, *378*, 87.
[15] J. Lee, O. K. Farha, J. Roberts, K. A. Scheidt, S. T. Nguyen, J. T. Hupp, *Chem. Soc. Rev.* **2009**, *38*.
[16] J. W. Maina, C. Pozo-Gonzalo, L. Kong, J. Schütz, M. Hill, L. F. Dumée, *Mater. Horiz.* **2017**, *4*.
[17] K. Sumida, D. L. Rogow, J. A. Mason, T. M. McDonald, E. D. Bloch, Z. R. Herm, T.-H. Bae, J. R. Long, *Chem. Rev.* **2012**, *112*, 724.
[18] H. Furukawa, F. Gándara, Y.-B. Zhang, J. Jiang, W. L. Queen, M. R. Hudson, O. M. Yaghi, *J. Am. Chem. Soc.* **2014**, *136*, 4369.
[19] O. I.-F. Chen, C.-H. Liu, K. Wang, E. Borrego-Marin, H. Li, A. H. Alawadhi, J. A. Navarro, O. M. Yaghi, *J. Am. Chem. Soc.* **2024**, *146*, 2835.
[20] J. E. Mondloch, W. Bury, D. Fairen-Jimenez, S. Kwon, E. J. DeMarco, M. H. Weston, A. A. Sarjeant, S. T. Nguyen, P. C. Stair, R. Q. Snurr, O. K. Farha, J. T. Hupp, *J. Am. Chem. Soc.* **2013**, *135*, 10294.
[21] P. Deria, J. E. Mondloch, E. Tylianakis, P. Ghosh, W. Bury, R. Q. Snurr, J. T. Hupp, O. K. Farha, *J. Am. Chem. Soc.* **2013**, *135*, 16801.
[22] V. Quezada-Novoa, H. M. Titi, A. A. Sarjeant, A. J. Howarth, *Chem. Mater.* **2021**, *33*.
[23] V. Quezada-Novoa, H. M. Titi, F. Y. Villanueva, M. W. B. Wilson, A. J. Howarth, *Small* **2023**, *19*, 2302173.
[24] J. M. Soler, E. Artacho, J. D. Gale, A. García, J. Junquera, P. Ordejón, D. Sánchez-Portal, *J. Condens. Matter Phys.* **2002**, *14*, 2745.
[25] M. Ernzerhof, G. E. Scuseria, *J. Chem. Phys.* **1999**, *110*, 5029.
[26] S. Grimme, *J. Comput. Chem.* **2006**, *27*, 1787.
[27] E. Sanville, S. D. Kenny, R. Smith, G. Henkelman, *J. Comput. Chem.* **2007**, *28*, 899.
[28] D. E. E. David Dubbeldam, S. Calero, R. Q. Snurr, *Mol. Simul.* **2016**, *42*, 81.

[29] M. G. Martin, J. I. Siepmann, *J. Phys. Chem. B* **1998**, *102*, 2569.
[30] A. K. Rappé, C. J. Casewit, K. Colwell, W. A. Goddard III, W. M. Skiff, *J. Am. Chem. Soc.* **1992**, *114*, 10024.
[31] S. L. Mayo, B. D. Olafson, W. A. Goddard, *J. Phys. Chem.* **1990**, *94*, 8897.
[32] A. Y. Toukmaji, J. A. Board Jr, *Comput. Phys. Commun.* **1996**, *95*, 73.
[33] D. Ongari, P. G. Boyd, O. Kadioglu, A. K. Mace, S. Keskin, B. Smit, *J. Chem. Theo. Comput.* **2018**, *15*, 382.
[34] A. K. Rappe, W. A. Goddard III, *J. Phys. Chem.* **1991**, *95*, 3358.
[35] D. Dubbeldam, S. Calero, T. J. Vlugt, *Mol. Simul.* **2018**, *44*, 653.
[36] C. Copeman, H. A. Bicalho, M. W. Terban, D. Troya, M. Etter, P. L. Frattini, D. M. Wells, A. J. Howarth, *Chem. Commun.* **2023**, *59*, 3071.
[37] T. C. Wang, N. A. Vermeulen, I. S. Kim, A. B. Martinson, J. F. Stoddart, J. T. Hupp, O. K. Farha, *Nat. Protoc.* **2016**, *11*, 149.
[38] R. C. Klet, Y. Liu, T. C. Wang, J. T. Hupp, O. K. Farha, *J. Mater. Chem. A* **2016**, *4*, 1479.
[39] H. J. Jun, D. K. Yoo, S. H. Jhung, *J. CO2 Util.* **2022**, *58*, 101932.
[40] J. M. Park, D. K. Yoo, S. H. Jhung, *Chem. Eng. J.* **2020**, *402*, 126254.
[41] R. Hardian, S. Dissegna, A. Ullrich, P. L. Llewellyn, M.-V. Coulet, R. A. Fischer, *Chem. Eur. J.* **2021**, *27*, 6804.
[42] T. M. Rayder, F. Formalik, S. M. Vornholt, H. Frank, S. Lee, M. Alzayer, Z. Chen, D. Sengupta, T. Islamoglu, F. Paesani, K. W. Chapman, R. Q. Snurr, O. K. Farha, *J. Am. Chem. Soc.* **2023**, *145*, 11195.
[43] C. Copeman, H. A. Bicalho, M. W. Terban, D. Troya, M. Etter, P. L. Frattini, D. M. Wells, A. J. Howarth, *Chem. Commun.* **2023**, *59*, 3071.
[44] N. Planas, J. E. Mondloch, S. Tussupbayev, J. Borycz, L. Gagliardi, J. T. Hupp, O. K. Farha, C. J. Cramer, *J. Phys. Chem. Lett.* **2014**, *5*, 3716.
[45] T. Islamoglu, K.-i. Otake, P. Li, C. T. Buru, A. W. Peters, I. Akpinar, S. J. Garibay, O. K. Farha, *CrystEngComm* **2018**, *20*, 5913.
[46] F. H. Allen, R. Taylor, *Chem. Soc. Rev.* **2004**, *33*, 463.
[47] W. Zhang, Y. Ma, I. A. Santos-López, J. M. Lownsbury, H. Yu, W.-G. Liu, D. G. Truhlar, C. T. Campbell, O. E. Vilches, *J. Am. Chem. Soc.* **2018**, *140*, 328.
[48] S. Pandey, B. Demaske, O. A. Ejegbavwo, A. A. Berseneva, W. Setyawan, N. Shustova, S. R. Phillpot, *Comput. Mater. Sci.* **2020**, *184*, 109903.
[49] S. G. Chen, R. T. Yang, *Langmuir* **1994**, *10*, 4244.
[50] A. Jain, S. P. Ong, G. Hautier, W. Chen, W. D. Richards, S. Dacek, S. Cholia, D. Gunter, D. Skinner, G. Ceder, K. A. Persson, *APL Mater.* **2013**, *1*, 011002.

Manuscript received: November 16, 2024
Revised manuscript received: February 4, 2025
Accepted manuscript online: February 25, 2025
Version of record online: March 27, 2025